

Observation of thermospheric gravity waves in the Southern Hemisphere with GOLD

Scott L England¹, Katelynn R Greer², Stanley C. Solomon³, Richard Eastes⁴, William E. McClintock², and Alan G. Burns³

¹Virginia Polytechnic Institute and State University

²University of Colorado Boulder

³National Center for Atmospheric Research (UCAR)

⁴Laboratory for Atmospheric and Space Physics

November 28, 2022

Abstract

The middle thermosphere from ~150 to 250 km is characterized by rapid increase in temperature with altitude and rapid ionization. The entire thermosphere is believed to be home to atmospheric waves that propagate through it, originating both in the atmospheric layers below and in the thermosphere itself. Within the middle thermosphere, direct observations of such waves are extremely sparse. The GOLD far-UV imaging spectrometer is able to observe the middle thermosphere from geostationary orbit. During October 2018 a special observational campaign was performed, designed to identify atmospheric waves. Signatures in the 135.6 nm O airglow were seen that move northwards with time, away from the Southern polar region. These are consistent with a large-scale atmospheric gravity wave. These results are the first time 135.6 nm airglow has been used to track such a wave and highlight the ability of GOLD to observe such waves, even when at a modest amplitude, and track their motion.

22 [Abstract](#)

23 The middle thermosphere from ~150 to 250 km is characterized by rapid increase in temperature
24 with altitude and rapid ionization. The entire thermosphere is believed to be home to atmospheric
25 waves that propagate through it, originating both in the atmospheric layers below and in the
26 thermosphere itself. Within the middle thermosphere, direct observations of such waves are
27 extremely sparse. The GOLD far-UV imaging spectrometer is able to observe the middle
28 thermosphere from geostationary orbit. During October 2018 a special observational campaign
29 was performed, designed to identify atmospheric waves. Signatures in the 135.6 nm O airglow
30 were seen that move northwards with time, away from the Southern polar region. These are
31 consistent with a large-scale atmospheric gravity wave. These results are the first time 135.6 nm
32 airglow has been used to track such a wave and highlight the ability of GOLD to observe such
33 waves, even when at a modest amplitude, and track their motion.

34

35 [Plain Language Summary](#)

36 The upper region of the Earth's atmosphere, stretching from around 90 – 500 km above the
37 surface, is known as the thermosphere. In this region, the temperature generally increases with
38 altitude, but the strongest increase is in a region known as the middle thermosphere. The main
39 source of heating in this region is absorption of ultraviolet light from the sun, which also
40 produces charged particles in this region, known as the ionosphere. Oscillations are observed in
41 almost all the properties of the atmosphere at these altitudes, which are believed to result from
42 waves within the atmosphere. In the middle thermosphere, there are very few direct observations
43 of such waves. GOLD is a new instrument that can observe the middle thermosphere by
44 measuring emissions from the atmosphere call airglow. During a day in October 2018, GOLD

45 observed what appear to be fluctuations in this airglow associated with such waves. The
46 properties are determined, both from the GOLD observations, and a theoretical model.

47

48 1) Introduction

49 The middle thermosphere, from around 150 to 250 km altitude, is characterized by a rapid
50 increase in temperature and changing atmospheric composition with altitude, high rates of
51 photoionization and associated generation of photoelectrons. As in much of Earth's atmosphere,
52 atmospheric waves are believed to play a key role in the dynamics of this region (e.g. Forbes,
53 2007). The spectrum of waves is observed to change at middle thermosphere altitudes, from the
54 relatively small vertical wavelengths (10s km) seen in the mesosphere and lower thermosphere
55 (MLT) to the relatively long vertical wavelengths (>100 km) seen in the upper thermosphere
56 (e.g. Oliver *et al.*, 1997; Djuth *et al.*, 2010). Atmospheric gravity waves (GWs) are believed to be
57 a key component of the wave spectrum in the middle thermosphere, and significantly impact this
58 region, both in creating transient variations and in producing net acceleration, mixing, heating
59 and heat flux as they dissipate (e.g. Yiğit and Medvedev, 2015). The GWs in the middle
60 thermosphere are believed to be a mixture of waves originating in the lower regions of the
61 atmosphere (both primary and secondary waves; e.g. Vadas and Fritts, 2006; Vadas and Liu,
62 2009; Yiğit *et al.*, 2014) as well as waves generated in the thermosphere, primarily via Joule
63 heating in the auroral regions (e.g. Richmond, 1978).

64

65 GWs in the MLT region have been observed frequently via a variety of methods, including
66 images of airglow (e.g. Swenson and Mende, 1994), lidar (e.g. Wilson *et al.*, 1991), radar (e.g.

67 Vincent and Fritts, 1987), observations of noctilucent clouds (e.g. Thurairajah *et al.*, 2017), and
68 limb profiles from low-earth orbit spacecraft (e.g. Preusse *et al.*, 2009). GWs have also been
69 detected frequently with *in situ* observations in the upper thermosphere (e.g. Bruinsma and
70 Forbes, 2008; Park *et al.* 2014; Garcia *et al.*, 2016). Despite the strong impacts GWs are believed
71 to have in the middle thermosphere (e.g. Vadas and Fritts, 2006; Vadas and Liu, 2009; Yiğit *et*
72 *al.*, 2014), very few direct observations of GWs in this region have been made. The vast majority
73 of observations of GW at middle thermosphere altitudes come from radar observations of
74 electron density or motion, which identify travelling ionospheric disturbances (TIDs) that are the
75 ionospheric counterpart to the GW in the neutral atmosphere (e.g. Djuth *et al.*, 2010; Negrea *et*
76 *al.*, 2016). Where observations of both the GW and TID have been made in the same location in
77 the thermosphere, it has been shown that the TID may be a very good proxy for the underlying
78 neutral GW (e.g. Earle *et al.*, 2008), and thus observations of TIDs may provide a great deal of
79 insight into the spectrum of GWs at this altitude, even if they don't reveal all the changes in the
80 neutral atmosphere associated with the GW. Using a combination of ionospheric (airglow
81 brightness) and thermospheric wind observations, Paulino *et al.*, 2018 were able to deduce the
82 intrinsic parameters of gravity waves in the middle thermosphere / bottom-side F-region and
83 confirm that the waves seen in the ionospheric response were consistent with upward
84 propagating gravity waves that are filtered by the background winds, both at these altitudes and
85 below.

86

87 Determining the characteristics of GWs in the thermosphere is important for understanding the
88 energy and momentum balance of this region. As just one example, it is believed that gravity

89 waves propagated upwards from below can either heat or cool the thermosphere (e.g. Yiğit and
90 Medvedev, 2009; Vadas *et al.*, 2014), but their impact on the thermosphere depends on their
91 properties, as well as the mean state. The characteristics of TIDs observed are typically grouped
92 into two categories according to their horizontal spatial scales. Medium scale TIDs (MSTIDs),
93 with horizontal wavelengths around 100 – 500 km, and horizontal phase speeds of around 100 –
94 200 m/s are believed to be associated with primary or secondary GWs from the lower levels of
95 the atmosphere (e.g. Azeem *et al.*, 2017), whereas large scale TIDs (LSTIDs), with horizontal
96 wavelengths over 1000 km, and horizontal phase speeds of around 500 m/s are believed to be
97 associated with aurorally-generated GWs (e.g. Bruinsma *et al.*, 2006). Given the importance of
98 GWs in the middle thermosphere, and the comparative lack of direct observations of these waves
99 in this region, further examination of observations of GWs in the neutral atmosphere at these
100 altitudes is warranted.

101

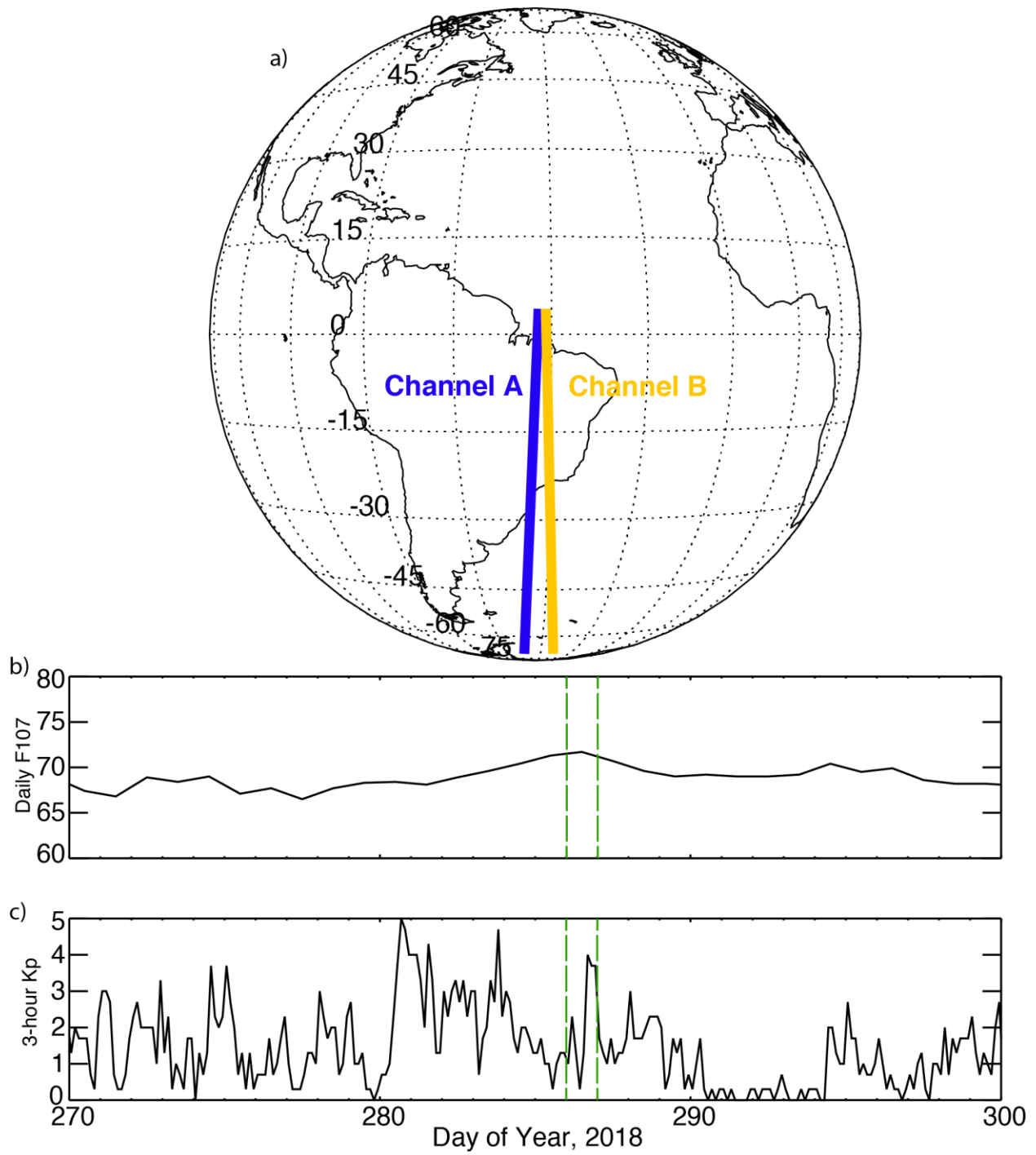
102 Global-scale Observations of the Limb and Disk (GOLD) is a NASA Mission of Opportunity,
103 primarily focused on observing the far-ultraviolet airglow emissions from the Earth's middle
104 thermosphere and F-region ionosphere. Here we present the results from a special campaign of
105 observations from GOLD, designed to reveal the impacts of GWs on the airglow originating
106 from the middle thermosphere. While this dataset is unique in that it represents a special
107 campaign that has yet to be repeated, these results will highlight the capabilities of the GOLD
108 instrument to observe such waves. We identify the impact GWs on the FUV airglow during a
109 geomagnetically quiet to moderate day, analyze the GOLD observations and make use of an

110 airglow model to estimate the intrinsic wave parameters in the neutral atmosphere. These results
111 can also be used to help define future campaigns with the GOLD instrument.

112

113 2) Experimental Setup and Data

114 GOLD is a 2-channel far-ultraviolet imaging spectrometer that observes the Earth from onboard
115 the SES-14 geostationary communications satellite, which is located at 312.5° longitude (Eastes
116 *et al.*, 2017; McClintock *et al.*, 2017; Eastes *et al.*, 2019). During regular operations, when the
117 disk of the Earth is illuminated by the sun, the instrument scans the disk of the Earth, building up
118 an image of the Earth's disk with a 30-minute cadence. GOLD makes observations between
119 ~134 and 167 nm, which allows identification of the prominent dayglow features of O at 135.6
120 nm and LBH band of N₂. During early operations on October 13, 2018, both channels of the
121 instrument performed a special mode campaign, designed to identify the impacts of atmospheric
122 waves on the middle thermosphere. Based on modeling by Greer *et al.*, [2018], the anticipated
123 changes in O dayglow at 135.6 nm were of order ± 2 Rayleighs, requiring an integration time of
124 ~400 s to clearly identify such perturbations, which is much longer than the typical dwell time
125 when scanning the disk. To maximize the chance of seeing such a perturbation in the airglow, the
126 special mode campaign involved pointing both channels close to nadir, with the mirror position
127 set to view the southern hemisphere and stare continuously from ~12 – 18 hours UTC (see
128 Figure 1a). As the two channels are mounted in opposite directions on the spacecraft, the tilt of
129 the slit with latitude is in the opposite direction for each channel such that the longitudinal
130 separation of the fields of view is $\sim 1^\circ$ at the equator, increasing to $\sim 9.9^\circ$ towards the edge of the
131 disk at -61° latitude. It is this, currently unique ~6-hour long dataset that will be considered here.



132

133 *Figure 1: Panel a shows the fields of view of Channel A and B of GOLD during the special mode*

134 *campaign on October 13, 2018. Panel b shows daily F10.7 index and panel c shows the 3-hourly*

135 *K_p index around the time of this campaign, with October 13, 2018 highlighted by the vertical*
136 *dashed lines.*

137

138 While the special mode campaign was pre-planned and not intended to align with any specific
139 geophysical conditions, the conditions present on October 13, 2018 were geomagnetically quiet
140 to moderate. Figure 1b and 1c show the F10.7 and K_p indices during this period of 2018. F10.7
141 values on the day was low at $71.7 \cdot 10^{-22} \text{ W m}^{-2} \text{ Hz}^{-1}$, while the K_p values show moderate activity,
142 reaching 4+ by later in the day. Examining the real-time auroral AE index shows activity below
143 100 nT from 12 – 15 UT, with a pickup between 15 – 18 UT up to over 1200 nT by the end of
144 the period. It is worth noting that this heightened activity occurred several hours into the
145 campaign.

146

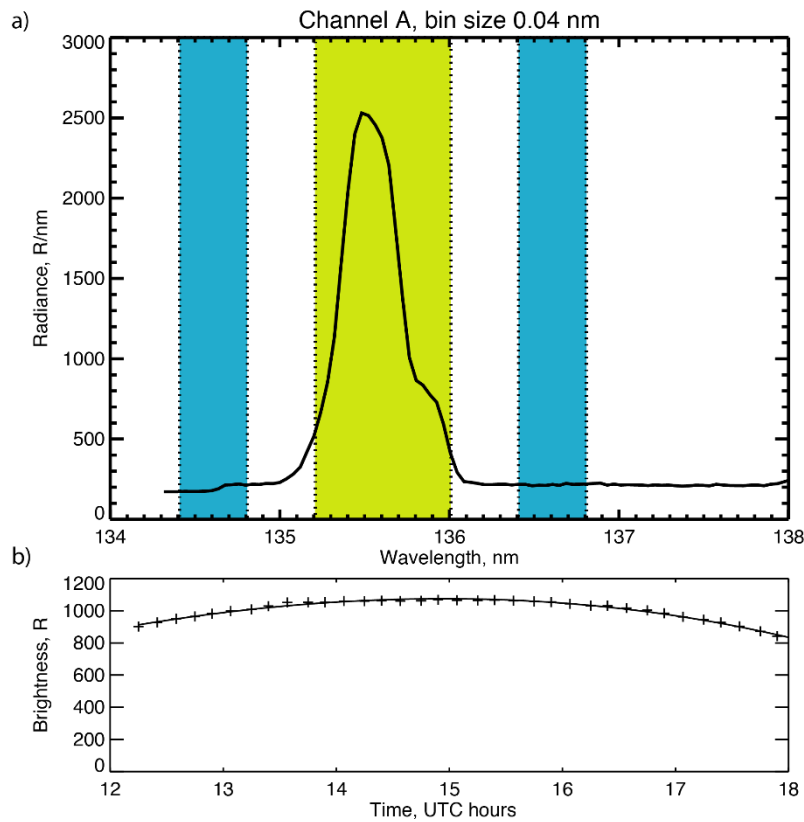
147 This study focuses on Level 1b and 1c (L1b & L1c) data from the GOLD instrument, which are
148 described in the Data Products Users Guide (see <https://gold.cs.ucf.edu>). The L1b files are
149 available for this campaign at 2-minute cadence and provide the spectrum in instrument counts
150 vs wavelength and latitude. The L1b processing includes geometric corrections for the detector
151 and optics, filtering of the counts based on the detector pulse heights, a correction based on the
152 detector deadtime (maximum count rate) and data are binned on a regular wavelength scale. The
153 L1c files are available at a 10-minute cadence and provide the spectrum in radiance vs
154 wavelength and latitude. The L1c processing additionally includes the radiometric conversion
155 based on knowledge of the instrument flatfield response, scattered light and dark current noise
156 sources, and sensitivity vs wavelength.

157

158 3) Data Analysis

159 Given the low amplitude of the signal expected from an atmospheric gravity wave described
160 above, our analysis focuses on the bright O doublet feature near 135.6 nm, although it is worth
161 noting that this overlaps the (3,0) emission from N₂ at 135.4 nm. Some of this can be excluded
162 by not including the shortest wavelength bins in our computation of the 135.6 nm feature, as has
163 been done here. To identify the perturbations associated with any atmospheric fluctuations such
164 as gravity waves, we first isolate the 135.6 nm airglow from the background, then detrend the
165 variations associated with changes in local time and any that may be associated with changes in
166 solar EUV brightness. This is done in three steps. To isolate the 135.6 nm airglow, we add up the
167 signal at each pixel at each point in time in the range from 135.2 – 136.0 nm, and perform a
168 background subtraction using two out of band regions either side of this, at 134.4 – 134.8 and
169 136.4 – 136.8 nm (see Figure 2a). To remove the local time variations, a third-order polynomial
170 fit is made to the signal at each pixel in each channel, and this smoothly varying signature is
171 removed (see Figure 2b). Finally, changes associated with varying solar EUV brightness affect
172 the signal at all latitudes on the disk simultaneously. As such, these are easily identified and
173 removed by finding and removing the mean value of brightness across the image, after the local
174 time variation is removed. This leaves a residual signal whose mean value is zero.

175



176

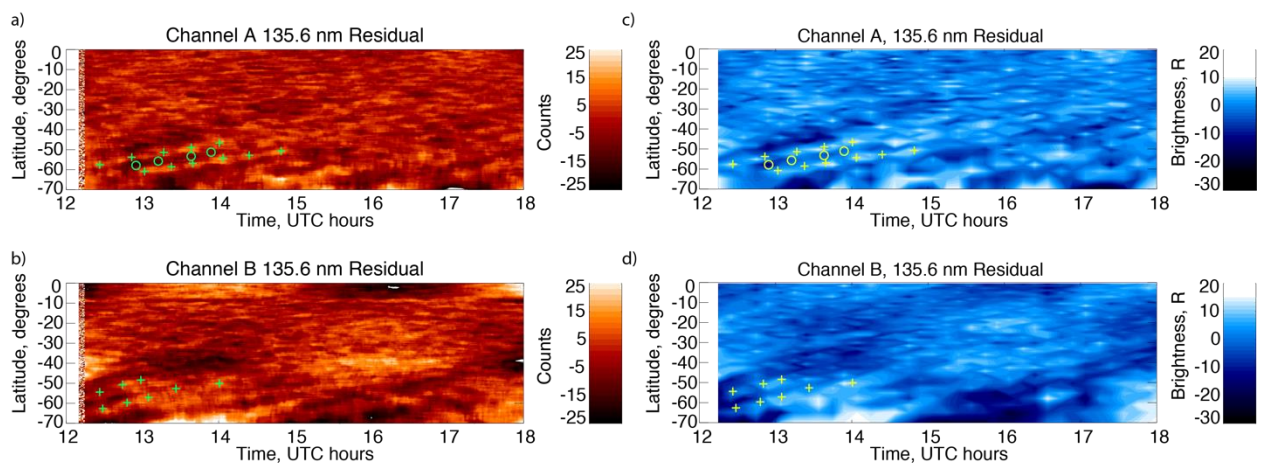
177 *Figure 2: Panel a shows an example spectrum from the L1c data from Channel A at -39°*
 178 *latitude, 12:49 – 12:58 UTC. The area highlighted in green represents the in-band and those in*
 179 *blue represent the out-of-band signals used in the analysis. Panel b shows the variation in the*
 180 *135.6 nm signal as a function of time for the same pixel shown in panel a. The plus symbols*
 181 *represent the L1c values at 10-minute cadence, and the solid line shows the 3rd order polynomial*
 182 *least-squares fit to these data.*

183

184 The atmospheric wave perturbations that may be expected in the middle thermosphere have
 185 periods of 10s of minutes to several hours, so both the 2-minute cadence L1b and 10-minute
 186 cadence L1c data should have sufficient temporal resolution to capture these. At this 2-minute
 187 cadence, the L1b residuals are extremely noisy. To allow any longer-period signatures to be

188 seen, we perform a 10-minute rolling median filter on these residuals at each latitude. This
 189 removes outlying high and low data points, and puts these data on approximately the same
 190 temporal resolution as the L1c file. Figure 3 shows residuals for L1b and L1c for 2 channels,
 191 after this median filter applied to L1b. In the residuals from both channels and both the L1b and
 192 L1c data, perturbations that appear to move northwards with time are seen. Perhaps most clearly
 193 visible are a pair of higher count rates / brightnesses features between 12 – 14 hours UTC near -
 194 50 – -65° latitude. The locations of these were determined by eye and their locations are given in
 195 Table 1.

196



197

198 *Figure 3: Panels a and b show the residual counts as defined in the text in the L1b data for*
 199 *Channels A and B respectively as functions of time and latitude. A 10-minute rolling median*
 200 *filter has been applied at each latitude for the L1b data. Panels c and d are as a and b, but for*
 201 *the brightness in Rayleighs from the L1c data. The locations of the apparent wave features,*
 202 *marked by the plus and circle symbols, are given in the Supplementary Data.*

203

Channel	Feature	Time, UTC hours	Latitudes, degrees
A	First	12.44	-57.52

	wave peak	12.86	-53.78
		13.28	-51.34
		13.64	-48.9
		14.01	-46.63
A	Second wave peak	13.03	-60.77
		13.38	-58.49
		13.66	-56.87
		14.06	-54.27
		14.4	-52.81
		14.82	-50.69
A	Trough	12.91	-57.71
		13.21	-55.57
		13.64	-53.13
		13.9	-51.1
B	First wave peak	12.48	-62.63
		12.8	-59.63
		13.08	-57.14
		13.44	-52.64
		14.01	-50.05
B	Second wave peak	12.44	-54.39
		12.84	-50.64
		13.08	-48.4

204 Table 1: The locations of the wave peak and trough feature highlighted in Figure 3.

205

206 Assuming that the two channels are seeing the same feature in the atmosphere, which seems
207 reasonable given the apparent similarity for the pair of features described above, and furthermore
208 assuming this to be an atmospheric wave with plane wave fronts, it is possible to estimate a
209 number of wave parameters. The mean residual brightness at the peak locations in Channel A for
210 the first wave is 3.4 R and for the second wave is 6.0 R. The mean residual brightness for the
211 trough between these waves is -5.9 R. The mean observed brightness in this region is 1180 R,
212 so using the average of the two peaks and the trough values listed above, the wave amplitude is
213 around 0.45 % , or 10.6 R. Performing a linear least-squares fit to the locations of the peaks of
214 these two waves in both channels, we can determine the wave period by the time between the

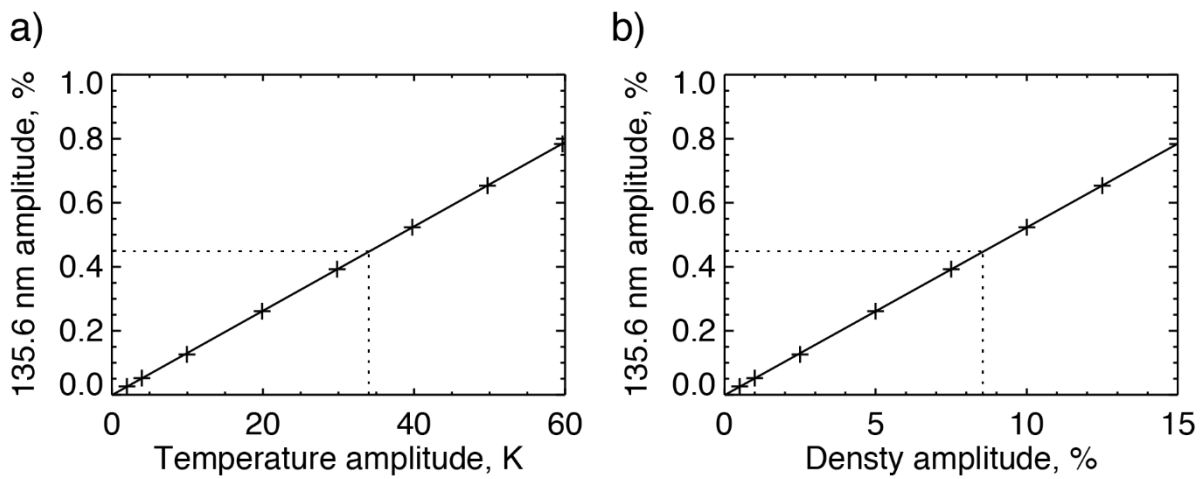
215 two peaks arriving at -52° latitude (chosen as both channels see both waves in this region). The
216 estimated wave period from Channel A is 1.3 hours and from Channel B is 1.0 hours, with a
217 mean of 1.2 hours. From the same linear fits, the meridional phase speed is estimated to be $7.6^\circ /$
218 hour northwards or ~ 230 m/s. The peaks of the waves appear to reach -52° latitude 0.7 hours
219 earlier in Channel B than Channel A. Combining this with the longitudinal separation of
220 Channels A and B at this latitude being 7.7° leads to an estimate of the zonal phase speed as $11^\circ /$
221 hour westwards or ~ 270 m/s. Using the meridional and zonal phase speeds, the total horizontal
222 phase speed is estimated to be 360 m/s, with an azimuth of wave propagation of 300° . From the
223 phase speeds and period, the horizontal wavelength is estimated to be ~ 1500 km. These wave
224 properties will be discussed further in Sections 4 and 5.

225

226 4) Airglow simulations

227 From the measured amplitude of the brightness perturbation, it is possible to estimate the
228 amplitude of a gravity wave that would be required to produce such a signature. Following the
229 methodology of Greer *et al.*, [2018], we use a background atmosphere from the thermosphere-
230 ionosphere-electrodynamics GCM (TIEGCM v2.0; Maute, 2017) and the Global Airglow model
231 (GLOW; Solomon, 2017) to simulate the 135.6 nm O and (3,0) N₂ airglow GOLD would
232 observe at -50° latitude for the conditions present on October 13, 2018. This is then perturbed
233 with a sinusoidal function that modifies the atmospheric density and temperature, as described in
234 Section 2 of Greer *et al.*, [2018]. By varying the amplitude of this perturbation, we can find the
235 amplitude of a wave in the middle thermosphere that would produce a perturbation in the airglow
236 of the same amplitude as observed by GOLD. Figure 4 shows the results of seven simulations at

237 varying wave amplitude, at both 9 am and 12 pm local time (corresponding approximately to 12
 238 and 15 UT in the GOLD observations). At these relatively small-amplitude perturbations in the
 239 atmosphere, the response in the airglow is very close to linear, and a linear least-squares fit is
 240 used to identify the best-fit wave amplitude that corresponds to the observed airglow signature.
 241 The 10.6 R or 0.9 % peak-to-trough variation seen by GOLD near these local times could be
 242 explained by a wave with an amplitude of 34 K, corresponding to 8.5 % density fluctuation.



243
 244 *Figure 4: Results of the GLOW airglow simulations of the O 135.6 nm double and N₂ (3,0) at -*
 245 *50° latitude for the conditions present on October 13, 2018. The amplitude of the simulated*
 246 *airglow perturbation is shown as a function of the change in the neutral atmosphere, expressed*
 247 *in terms of (panel a) the temperature and (panel b) the density perturbations. Simulations*
 248 *correspond to an average of 12:00 and 15:00 UT. The solid lines show the linear least-squares*
 249 *fit to these data. The dotted line shows the amplitude of the airglow perturbation observed by*
 250 *GOLD.*

251
 252 It is worth noting that the 135.6 nm O dayglow also includes a minor contribution from O⁺
 253 radiative recombination. This is expected to be small at -50° latitude, but nonetheless it is worth

254 determining if an ionospheric perturbation, either instead of in addition to an atmospheric
255 perturbation could explain the GOLD observations. Using an estimate of the ionospheric O^+
256 density in the region of the observed wave from IRI-2016 (Bilitza, 2018), and the radiative
257 recombination airglow coefficients from Meléndez-Alvira *et al.*, (1999), the total brightness of
258 O^+ radiative recombination near 12 UT is estimated to be 20 R. Thus, only an extremely large
259 amplitude variation in O^+ in the ionosphere could produce the 10.6 R variation seen by GOLD.
260 While it is likely that some portion of the observed signature is associated with ionospheric O^+
261 perturbations, it seems likely that the majority of the observed signal is associated with variations
262 in the neutral middle thermosphere.

263

264 5) Discussion and Conclusions

265 During the observing campaign on October 13th, 2018, GOLD observed perturbations in the
266 135.6 nm dayglow in the Southern hemisphere. These perturbations in the brightness of the
267 airglow were seen to move northwards with time and were seen with both channels of the
268 instrument, providing confidence that they represent the response to structures in the
269 thermosphere. The structures appear to be atmospheric gravity waves, or TAD, and if so this
270 would be the first time that the properties of such waves, including their propagation, have been
271 identified in 135.6 nm airglow. Using data from both channels, and approximating the wave as
272 plane wave it is possible to identify the best-fit horizontal wavelength of 1500 km, period of 1.2
273 hours, phase speed of 360 m/s and azimuth of propagation of 300°. These characteristics are
274 broadly consistent with those reported for large-scale TADs seen in the upper thermosphere (e.g.
275 Bruinsma *et al.*, 2006), and the larger scale TIDs seen in the ionosphere at middle-thermosphere
276 altitudes (e.g. Negrea *et al.*, 2016). Utilizing a model of the airglow, it is possible to estimate the

277 approximate amplitude of the atmospheric perturbation associated with this wave. The best fit to
278 the observed airglow perturbation was found from a wave in the neutral atmosphere with a
279 temperature amplitude of 33 K and a density amplitude of 8.5 %, which is consistent with *in situ*
280 observations of TADs in the middle – upper thermosphere (e.g. Earle *et al.*, 2008).

281

282 The direction of propagation suggests a wave source that is south and east of the observed
283 region, i.e. to the east of the Antarctic Peninsula. The GOLD data does not uniquely identify the
284 wave source, but there are perhaps three types broad source locations one could consider
285 – gravity waves of tropospheric origin (primary gravity waves), secondary gravity waves
286 produced at some higher altitude where a primary wave dissipates, or waves of thermospheric
287 origin. As described in Azeem *et al.*, [2017] (following Vadas, 2013), the maximum phase speed
288 for a wave of tropospheric origin is around 255 m/s, which appears to exclude this as the direct
289 origin of the wave observed by GOLD, leaving the other two as possibilities in this case.
290 Comparison to other observations, such as from ground-based instrumentation would be one
291 possible way to determine the wave source, but is beyond the scope of this study.

292

293 The results highlight the ability of GOLD to observe atmospheric waves. From its geostationary
294 vantage point, GOLD is perhaps ideally suited to tracking such waves over large horizontal
295 distances. The ability to detect a wave of relatively modest amplitude, not in response to a
296 geomagnetic storm, suggests opportunities for similar observing campaigns to be planned in the
297 future. GOLD's field of regard includes several regions believed to be important sources of
298 atmospheric gravity waves, including the Andes mountain range, the Antarctic Peninsula and
299 strong convective sources over the Amazon rainforest.

300

301 Acknowledgements, Samples and Data

302 The GOLD data are available from the GOLD Science Data Center

303 (<http://gold.cs.ucf.edu/search/>) and NASA's Space Physics Data Facility

304 (<https://spdf.gsfc.nasa.gov>). The Kp and F10.7 data are available from NASA's OMNIWeb

305 (<https://omniweb.gsfc.nasa.gov>). The IRI-2016 calculations were performed using NASA's

306 CCMC (<https://ccmc.gsfc.nasa.gov>). the AE real-time data are available from

307 http://wdc.kugi.kyoto-u.ac.jp/ae_realtime/201810/index_20181013.html. This research was

308 supported by NASA contract 80GSFC18C0061.

309

310 6) References

- 311 • Azeem, I., S. L. Vadas, G. Crowley, and J. J. Makela (2017), Traveling ionospheric
312 disturbances over the United States induced by gravity waves from the 2011 Tohoku tsunami
313 and comparison with gravity wave dissipative theory, *J. Geophys. Res. Space Physics*, 122,
314 3430–3447, doi:10.1002/2016JA023659.
- 315 • Bilitza, D. (2018), IRI the International Standard for the Ionosphere, *Adv. Radio Sci.*, 16, 1-
316 11, <https://doi.org/10.5194/ars-16-1-2018>.
- 317 • Bruinsma, S., J. M. Forbes, R. S. Nerem, and X. Zhang (2006), Thermosphere density
318 response to the 20–21 November 2003 solar and geomagnetic storm from CHAMP and
319 GRACE accelerometer data, *J. Geophys. Res.*, 111, A06303, doi:10.1029/2005JA011284.
- 320 • Bruinsma, S. L., & Forbes, J. M. (2008). Medium- to large-scale density variability as
321 observed by CHAMP. *Space Weather*, 6, S08002. <https://doi.org/10.1029/2008SW000411>

- 322 • Djuth, F. T., L. D. Zhang, D. J. Livneh, I. Seker, S. M. Smith, M. P. Sulzer, J. D. Mathews,
323 and R. L. Walterscheid (2010), Arecibo’s thermospheric gravity waves and the case for an
324 ocean source, *J. Geophys. Res.*, 115, A08305, doi:10.1029/2009JA014799.
- 325 • Earle, G. D., A. M. Musumba, and S. L. Vadas (2008), Satellite-based measurements of
326 gravity wave-induced midlatitude plasma density perturbations, *J. Geophys. Res.*, 113,
327 A03303, doi:10.1029/2007JA012766.
- 328 • Eastes, R. W., McClintock, W. E., Burns, A. G., Anderson, D. N., Andersson, L., Codrescu,
329 M., et al. (2017). The Global-Scale Observations of the Limb and Disk (GOLD) mission.
330 *Space Science Reviews*, 212(1-2), 383–408. <https://doi.org/10.1007/s11214-017-0392-2>
- 331 • Eastes, R. W., Solomon, S. C., Daniell, R. E., Anderson, D. N., Burns, A. G., England, S. L.,
332 et al. (2019). Global-scale observations of the equatorial ionization anomaly. *Geophysical*
333 *Research Letters*, 46. <https://doi.org/10.1029/2019GL084199>
- 334 • Forbes, J.M. (2007). Dynamics of the Thermosphere, *Journal of the Meteorological Society*
335 of Japan, Vol. 85B, pp. 193—213.
- 336 • Garcia, R. F., Bruinsma, S., Massarweh, L., & Doornbos, E. (2016). Medium-scale gravity
337 wave activity in the thermosphere inferred from GOCE data. *Journal of Geophysical*
338 *Research: Space Physics*, 121, 8089–8102. <https://doi.org/10.1002/2016JA022797>
- 339 • Greer, K. R., England, S. L., Becker, E., Rusch, D., & Eastes, R. (2018). Modeled gravity
340 wave-like perturbations in the brightness of far ultraviolet emissions for the GOLD mission.
341 *Journal of Geophysical Research: Space Physics*, 123, 5821–5830.
342 <https://doi.org/10.1029/2018JA025501>

- 343 • Maute, A., Thermosphere–ionosphere-electrodynamics general circulation model for the
344 Ionospheric Connection Explorer: TIEGCM-ICON. *Space Sci. Rev.* (2017),
345 doi:[10.1007/s11214-017-0330-3](https://doi.org/10.1007/s11214-017-0330-3)
- 346 • McClintock, W. E., et al. (2017), Global-scale Observations of the Limb and Disk (GOLD):
347 science implementation. American Geophysical Union Fall Meeting, SA31A-2561.
- 348 • Meléndez-Alvira, D. J., R. R. Meier, J. M. Picone, P. D. Feldman, and B. M. McLaughlin
349 (1999), Analysis of the oxygen nightglow measured by the Hopkins Ultraviolet Telescope:
350 Implications for ionospheric partial radiative recombination rate coefficients, *J. Geophys.*
351 *Res.*, 104, 14,901–14,914.
- 352 • Negrea, C., N. Zobotin, T. Bullett, T. Fuller-Rowell, T.-W. Fang, and M. Codrescu (2016),
353 Characteristics of acoustic gravity waves obtained from Dynasonde data, *J. Geophys. Res.*
354 *Space Physics*, 121, 3665–3680, doi:[10.1002/2016JA022495](https://doi.org/10.1002/2016JA022495).
- 355 • Oliver, W. L., Y. Otsuka, M. Sato, T. Takami, and S. Fukao (1997), A climatology of F
356 region gravity wave propagation over the middle and upper atmosphere radar, *J. Geophys.*
357 *Res.*, 102, 14,499.
- 358 • Park, J., Lühr, H., Lee, C., Kim, Y. H., Jee, G., & Kim, J.-H. (2014). A climatology of
359 medium-scale gravity wave activity in the midlatitude/low- latitude daytime upper
360 thermosphere as observed by CHAMP. *Journal of Geophysical Research: Space Physics*,
361 119, 2187–2196. <https://doi.org/10.1002/2013JA019705>
- 362 • Paulino, I., Moraes, J.F., Maranhão, G.K., Wrasse, C.M., Buriti, R.A., Medeiros, A.F.,
363 Paulino, A.R., Takahashi, H., Makela, J.J., Meriwether., J.W., and Compos, J.A.V. (2018),
364 Intrinsic parameters of periodic waves observed in the OI6300 airglow layer over the

- 365 Brazilian equatorial region, *Ann. Geophys.*, 36, 265-273m <https://doi.org/10.5194/angeo-36->
366 265-2018.
- 367 • Preusse, P., S. D. Eckermann, M. Ern, J. Oberheide, R. H. Picard, R. G. Roble, M. Riese, J.
368 M. Russell, and M. G. Mlynczak (2009), Global ray tracing simulations of the SABER
369 gravity wave climatology, *J. Geophys. Res.*, 114, D08126, doi:10.1029/2008JD011214.
- 370 • Richmond, A. D. (1978). Gravity wave generation, propagation, and dissipation in the
371 thermosphere. *Journal of Geophysical Research*, 83(A9), 4131–4145.
372 <https://doi.org/10.1029/JA083iA09p04131>
- 373 • Solomon, S. C. (2017). Global modeling of thermospheric airglow in the far ultraviolet.
374 *Journal of Geophysical Research: Space Physics*, 122, 7834–7848.
375 <https://doi.org/10.1002/2017JA024314>
- 376 • Swenson, G. R., and S. B. Mende, OH emission and gravity waves (including a breaking
377 wave) in all-sky imagery from Bear Lake, UT, *Geophys. Res. Lett.*, 21, 2239–2242, 1994.
- 378 • Thurairajah, B., Sato, K., Yue, J., Nakamura, T., Kohma, M., Bailey, S.M., and Russell III,
379 J.M. (2017). Simultaneous observation of gravity waves at PMC altitude from AIM/CIPS
380 experiment and PANSY radar over Syowa (69°S, 39°E), *J. Atmos. Sol. Terr. Phys.*, 164,
381 324-331, <https://doi.org/10.1016/j.jastp.2017.10.006>
- 382 • Vadas S.L., Fritts D.C. (2006) Influence of solar variability on gravity wave structure and
383 dissipation in the thermosphere from tropospheric convection. *J Geophys Res* 111:A10S12.
384 doi:10.1029/2005JA011510
- 385 • Vadas S.L., Liu H.-L. (2009) The generation of large-scale gravity waves and neutral winds
386 in the thermosphere from the dissipation of convectively-generated gravity waves. *J Geophys*
387 *Res* 114:A10310. doi:10.1029/2009JA014108

- 388 • Vadas, S. L. (2013), Compressible f-plane solutions to body forces, heatings, and coolings,
389 and application to the primary and secondary gravity waves generated by a deep convective
390 plume, *J. Geophys. Res. Space Physics*, 118, 2377–2397, doi:10.1002/jgra.50163.
- 391 • Vadas, S. L., Liu, H. L., & Lieberman, R. S. (2014). Numerical modeling of the global
392 changes to the thermosphere and ionosphere from the dissipation of gravity waves from deep
393 convection. *Journal of Geophysical Research: Space Physics*, 119(9), 7762-7793.
- 394 • Vincent, R. A., and D. C. Fritts, A climatology of gravity waves in the mesosphere and lower
395 thermosphere over Adelaide, Australia, *J. Atmos. Sci.*, 44, 748–760, 1987.
- 396 • Wilson, R., M.-L. Chanin, and A. Hauchecorne, Gravity waves in the middle atmosphere
397 observed by Rayleigh lidar, part 2, Climatology, *J. Geophys. Res.*, 96, 5169–5183, 1991
- 398 • Yiğit, E., & Medvedev, A. S. (2009). Heating and cooling of the thermosphere by internal
399 gravity waves. *Geophysical Research Letters*, 36(14).
- 400 • Yiğit, E. and A.S. Medvedev (2015). Internal wave coupling processes in Earth's
401 atmosphere, *Adv. Space Res.*, 55 (4) 983-1003, [10.1016/j.asr.2014.11.020](https://doi.org/10.1016/j.asr.2014.11.020)
- 402 • Yiğit, E., A. S. Medvedev, S. L. England, and T. J. Immel (2014), Simulated variability of
403 the high-latitude thermosphere induced by small-scale gravity waves during a sudden
404 stratospheric warming, *J. Geophys. Res. Space Physics*, 119, 357–365,
405 doi:10.1002/2013JA019283.